Materials and Interfaces
https://www.sciltp.com/journals/mi

Article

Size-Controlled Synthesis of Rhodium Nanocatalysts and Applications in Low-Temperature Hydroformylation

Andrew Lamkins [1,2], Charles J. Ward [1,2], Jeffrey T. Miller [3], Ziad Alsudairy [4], Xinle Li [4], Joseph Thuma [1,2], Ruoyu Cui [1,2], Xun Wu [1,2], Levi M. Stanley [1] and Wenyu Huang [1,2,*]

[1] Department of Chemistry, Iowa State University, Ames, IA 50010, USA
[2] Ames Laboratory, U.S. Department of Energy, Ames, IA 50010, USA
[3] Davidson School of Chemical Engineering, Purdue University, West Lafayette, IN 47907, USA
[4] Department of Chemistry, Clark Atlanta University, Atlanta, GA 30314, USA
* Correspondence: whuang@iastate.edu

How To Cite: Lamkins, A.; Ward, C.J.; Miller, J.T.; et al. Size-Controlled Synthesis of Rhodium Nanocatalysts and Applications in Low-Temperature Hydroformylation. *Materials and Interfaces* **2025**, *2*(1), Page Range. https://doi.org/10.xxxx/xxx.

Received: 3 December 2024
Revised: 30 December 2024
Accepted: 3 January 2025
Published: Day Month Year

Abstract: Controlling the size and distribution of metal nanoparticles is one of the simplest methods of tuning the catalytic properties of a material. For a nanocrystal particle, the ratio of edge-to-terrace sites can be critical in determining its catalytic activity and selectivity to desired products. To study these effects, we have developed a simple impregnation method of controlling the dispersion of rhodium atoms at the same metal loading in the range of nanoparticles less than 10 nm. Rh precursor salts are loaded onto inert SBA-15, and increasing the ratio of chloride to acetylacetonate salts improves the dispersion of rhodium atoms to form small Rh nanoparticles. Extensive characterization of the size-controlled catalysts, including XAS and in-situ CO-DRIFTS studies, has been performed to characterize the structure of Rh nanoparticles. Applying these catalysts to the hydroformylation of styrene, we observed that turnover frequency increases with decreasing particle size from 6.4 to 1.6 nm. When applied to hydroformylation reactions, we achieved a high branched product selectivity and successfully demonstrated a route to synthesizing the pain relief drug ibuprofen. This simple method can also synthesize Pt and Pd nanoparticles between 2–10 nm.

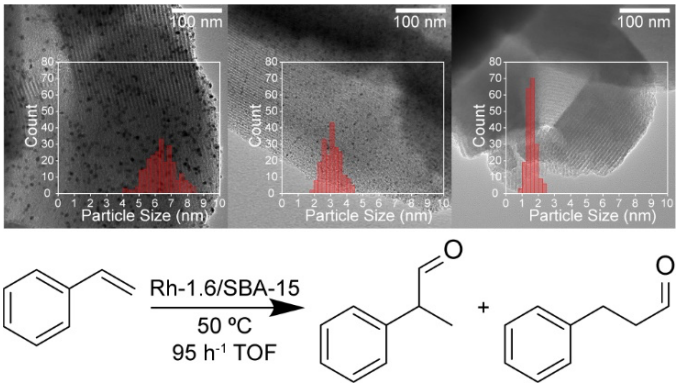

Keywords: heterogeneous catalysis; hydroformylation; EXAFS; infrared spectroscopy; nanoparticle

1. Introduction

The behavior of catalytic systems when varying nanoparticle (NP) size is one of the most studied areas in heterogeneous catalysis [1–10]. An effective method of size control is using capping agents during the synthesis of NPs [7,11], but the capping agents could compete with reactants for coordination to the NPs [12]. Using functional groups to anchor metals to support has the same issue of competitive adsorption [13]. Other methods of controlling NP size, such as inducing defects in the support to stabilize small NPs, are not broadly applicable and can't be used on an inert support like SiO_2. Changing the weight percent (wt.%) of metal on support is another broadly practiced method to alter the size of metal NPs, but it introduces further issues in evaluating catalysts. For example, controlling the space velocity of a reaction is an important factor in comparing catalysts, and differences in metal loading can affect how catalysis data can be interpreted, especially for kinetic studies in a flow reactor [14,15]. When metal loadings on support differ between catalysts, keeping the same amount of metal in the reactor will inevitably change the space velocity. Using catalysts with the same metal loading but different particle sizes is preferable to study the size effect of supported metal nanoparticles on catalysis.

Hydroformylation of olefins to aldehydes (the oxo process) has been a critical industrial reaction since its discovery in 1938 [13,16–18], and is now a vital part of the chemical production industry [19]. Homogeneous rhodium complexes are the prevailing industrial catalysts and are still being studied in modern research [20–22]. However, it is challenging to separate homogeneous catalysts from the reaction mixture, which reduces the overall recyclability of these catalysts [23–25]. The high cost of rhodium causes losses to add up quickly and makes designing alternative catalysts that are easier to recycle of paramount importance [16,20–22,25]. Heterogeneous catalysts, where the active site is at a solid-liquid interface, are far easier to separate than homogenous ones. The superior recyclability of heterogenous catalysts is preferred for industrial applications.

Typical hydroformylation also seeks a high yield to the n-aldehyde (linear) product over the iso-aldehyde (branched) product, though, in the hydroformylation of styrene (Scheme 1), the branched product is also valuable. The branched products of styrene hydroformylation have been used to study the enantioselective properties of catalysts [26]. When considering styrene derivates, such as 1-isobutyl-4-vinylbenzene, as the substrate, the branched aldehyde product from hydroformylation can serve as the precursor for (R/S)-2-(4-(isobutyl)phenyl)propanoic acid, commonly known as ibuprofen. Ibuprofen is a nonsteroidal anti-inflammatory medication that treats conditions such as inflammation-related diseases, pain, fever, and menstrual cramps.

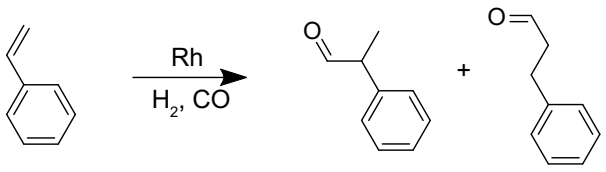

Scheme 1. Hydroformylation of styrene.

Efforts to study the impact of NP size during the hydroformylation of ethylene, 1-hexene, 1-decene, and even formaldehyde have provided insight into changes in activity, chemoselectivity, and regioselectivity in different particle size regimes [10,20,27–30]. In the hydroformylation of small molecules, like ethylene or formaldehyde, a volcano plot of NP size vs aldehyde turnover frequency (TOF) is observed, as the largest particles fail to achieve high activity due to a limited number of edge and corner sites, which are most active for hydroformylation. However, when NP size is too small, they predominantly catalyze the olefin hydrogenation rather than the hydroformylation [28–30]. This is contrasted by hydroformylation reports of larger molecules, which consistently have near 100% chemoselectivity to aldehydes regardless of particle size [12,13,18,27]. Despite the large body of literature on hydroformylation, we have found no reports of a dedicated effort to study the effect of NP size on the hydroformylation of styrene. The impact of NP size was briefly studied previously for Rh supported on silica gel [12]. However, the activity comparison between Rh NPs of different sizes is inconclusive because only the total amount of catalyst was kept constant in catalytic reactions instead of the Rh amount.

In this work, we have developed a general and scalable method for synthesizing metal NP catalysts across various sizes. Chloride ions have been reported to increase the dispersion of metal atoms during reduction from precursor salt to NPs [31]. Using $RhCl_3$ as a precursor leads to Rh NPs of 1.6 ± 0.3 nm, while the acetylacetonate salt gives Rh NPs of 6.4 ± 0.9 nm. By adjusting the ratio between the chloride and acetylacetonate metal precursors impregnated successively in mesoporous silica support, the size of Rh NPs can be controlled between 1.6 and 6.4 nm at the same Rh loading, ~3 wt.%. We employed these Rh-X/SBA-15 (X = particle size, nm) in the low-temperature hydroformylation of styrene. The smallest, Rh-1.6/SBA-15, displayed a TOF four times higher than

the homogeneous Wilkinson catalyst while matching the activity of previously reported single-atom catalysts [18]. We successfully performed hydroformylation of 1-isolbutyl-4-vinylbenzene to demonstrate a route to synthesize ibuprofen. Finally, this method of controlling metal NP size is also extended to synthesizing Pt and Pd particles with sizes ranging between ~2 to 10 nm.

2. Materials and Methods

2.1. Materials

Pluronic P123 and styrene (99%) were purchased from Sigma-Aldrich. Rhodium (III) chloride hydrate ($RhCl_3 \bullet xH_2O$, >99%) and rhodium (III) acetylacetonate ($Rh(acac)_3$, 97%) were purchased from Aldrich (Milwaukee, WI, USA). Chloridotris(triphenylphosphine)rhodium(I) (Wilkinson catalyst, >98%) was purchased from TCI (Tokyo, Japan). Syngas ($CO:H_2$ = 1:1) was purchased from Airgas (Waukesha, WI, USA). 4-isobutylbenzaldehyde (95%) was purchased from Combi Blocks (San Diego, CA, USA).

2.2. SBA-15 Synthesis

4 g of Pluronic P123, 130 mL water, and 20 mL 12.1 M HCl are mixed at 38 °C for 24 h in a 500 mL polypropylene (PP) bottle. 9.11 mL TEOS is added to the bottle quickly, still at 38 °C and with stirring, and allowed to react further for 20 h. The mixture sealed in the PP bottle is then placed in an oven at 100 °C for 24 h under static conditions. After cooling to room temperature, the white solid in the bottle was separated by filtration, washed with water, and further washed with ethanol three times. After drying at room temperature, the solid is calcined at 550 °C for 6 h before being stored in a desiccator until further use. We used a temperature ramping program for the calcination from a previous report [32].

2.3. Rh-X/SBA-15 Synthesis

Rh catalysts are prepared by incipient wetness impregnation [13]. For a typical synthesis of Rh-1.6/SBA-15, 50 µL of 0.3 M $RhCl_3$ aqueous solution is mixed thoroughly in a 1 dram vial with 50 mg SBA-15. After mixing for 5 min, ensuring that no dark regions are visible, the vial is capped and placed in a desiccator for > 8 h. Next, the solid is placed in an oven at 100 °C in air for 2 h to evaporate liquid water. The catalyst is then placed in a tube furnace, ramped at 5 °C/min to 200 °C, and kept for 2 h with 10% H_2 in Ar flowing at 50 mL/min. To synthesize Rh-6.4, the same procedure is followed using $Rh(acac)_3$ dissolved in chloroform. To make Rh-3.2/SBA-15, a 0.15 M solution of $Rh(acac)_3$ chloroform was impregnated first. The same steps are followed until after evaporating the solvent. Then, 0.15 M $RhCl_3$ aqueous solution is impregnated following the same procedure as the synthesis of Rh-1.6/SBA-15. To test if other Cl^- sources can have a similar size control effect, we impregnated 50 µL aqueous solution of 0.9 M KCl to $Rh(acac)_3$/SBA-15, then dried and reduced the sample as before.

2.4. Rh-X/SBA-15 Characterization

Powder X-ray diffraction (PXRD) measurements were collected with a Bruker D8 (Billerica MA, USA) Advance powder diffractometer with a Cu K_α radiation source (40 kV, 40 mA, λ = 1.5406 Å). Transmission electron microscopy (TEM) samples were prepared by drop-casting the catalyst suspension solution onto a carbon-coated copper grid. TEM images were obtained using a JEOL 2100 (Tokyo, Japan) transmission electron microscope operated at 200 kV. Scanning transmission electron microscopy (STEM) experiments were conducted using an FEI Titan Themis (Waltham, MA, USA), an aberration-corrected scanning transmission electron microscope at 200 kV. Inductively coupled plasma mass spectrometry (ICP-MS) measurements were performed using an Agilent 7700 Series spectrometer (Santa Clara CA, USA). Diffuse reflectance infrared Fourier transformed spectroscopy (DRIFTS) spectra were collected using a Bruker Vertex 80 FTIR (Billerica MA, USA) with a linearized mercury−cadmium−telluride detector, a Harrick diffuse reflectance accessory, and a Praying Mantis high-temperature reaction chamber. All spectra were obtained at a resolution of 2 cm^{-1} from 1000 to 4000 cm^{-1} under atmospheric pressure. Before measurement, a reducing pretreatment was used to clean catalyst surfaces. Catalysts were treated with 50 mL/min of 10% H_2 in He at 200 °C for 1 h to freshly reduce NPs and remove water. Samples were then cooled to 0 °C while purging with pure He at 20 mL/min. The background was then recorded as the spectrum of the sample under He. CO was flowed at 5 mL/min and diluted with 20 mL/min He for 20 min, after which CO was turned off, and He was kept flowing to flush out free CO. Sample spectra were collected 20 min after turning off CO flow. X-ray absorption spectroscopy (XAS) measurements were performed at beamline 8-ID ISS at the National Synchrotron Light Source II at Brookhaven National Laboratory. Data was

collected on the Rh K-edge in fluorescence mode. Scans were performed simultaneously at room temperature and collected with 30 s/scan; 10 scans were taken for each sample and merged for analysis. A Rh_2O_3 reference was also measured. Rh foil was obtained simultaneously with the sample spectra for energy calibration. The fraction of metallic and oxidized Rh was determined by fitting the sample XANES with Rh foil and Rh_2O_3 reference XANES. The k^2-weighted EXAFS data from k = 2.9 to 11.9 $Å^{-1}$ and r = 1.0 to 2.9 Å was fit in R-space using the WinXAS 4.0 software (Thorsten Ressler, Germany). Rh-O and Rh-Rh scattering paths were modeled using FEFF 6.0 software (University of Washington, Seattle, WA, USA). S_0 was determined by fitting Rh foil with 12 Rh-Rh at 2.68 Å. X-ray photoelectron spectroscopy (XPS) experiments were conducted by protecting the samples from air until they were ready for measurements. Samples were analyzed on a Thermo Scientific K-Alpha XPS apparatus (Waltham, MA, USA) equipped with a monochromatic Al K_α source and flood gun for charge compensation. XPS data fitting was conducted using Thermo Avantage software (Avantage 5.9931.0.6755, Thermo Fisher Scientific, Waltham, MA, USA). Temperature programmed reduction (TPR) using hydrogen was done in a fixed bed flow reactor connected to an Agilent 5975 inert mass selective detector, measuring m/z =36.5 ± 0.7. 250 mg of unreduced $RhCl_3$/SBA-15 was placed in the reactor and then heated at 5 °C/min starting at 30 °C for 2.5 h under a 10% H_2 in He flow at 50 mL/min. CO chemisorption was conducted using a Micromeritics 3Flex surface characterization analyzer at 35 °C. Samples were reduced at 200 °C for 1 h in pure hydrogen flow before analysis. The first isotherm was collected at 200 °C after evacuation for 30 min using a turbomolecular pump. The second isotherm was collected after evacuation at 35 °C for 1 h. The difference between the isotherms extrapolated to zero pressure is the amount of chemisorbed CO. Exposed Rh was calculated using CO/Rh = 1.5.

2.5. Catalytic Testing

In a typical run for hydroformylation, 0.5 mmol of styrene, 0.5 μmol Rh, and 2 mL of toluene were added to a 1-dram vial with a magnetic stir bar. Vials were placed in an aluminum heating block inside a stainless-steel autoclave and sealed. The air inside the autoclave is purged by flushing with syngas 5 times before charging to the reaction pressure of 30 bar. The autoclave is placed in an oil bath pre-heated to the desired temperatures and allowed to react for the specified time. Time starts when the autoclave is placed in the oil. Reaction mixtures were analyzed by gas chromatography (GC). An HP 6890 GC equipped with an HP-5 capillary column (30 m × 0.250 mm × 0.25 μm) and flame ionization detector were used to analyze the mixture after catalysis. Studies of activation energy, selectivity, and catalyst recycle tests were conducted by maintaining the conversion of styrene to less than 15%.

2.6. 1-isobutyl-4-vinylbenzene Synthesis

The 1-isobutyl-4-vinylbenzene was synthesized from 4-isobutylbenzaldehyde using the Wittig reaction according to a previously reported procedure [33].

3. Results and Discussion

A series of Rh NPs were encapsulated in the pores of SBA-15 via an incipient wetness impregnation method. Using $RhCl_3$, $Rh(acac)_3$, or their combination yielded different particle sizes upon reduction. The Rh loadings in all samples are around the target of 3 wt.% (Table 1). Rh-X/SBA-15 catalysts were characterized via TEM and STEM to obtain precise particle sizes based on counting >200 particles. The Rh NPs prepared from pure acetylacetonate, a 50:50 mixture of acetylacetonate and chloride, and pure chloride salts have diameters of 6.4 ± 0.9, 3.2 ± 0.6, and 1.6 ± 0.3 nm, respectively (Figure 1). PXRD results (Figure 2a) agree with STEM, where the crystalline size decreases as increased peak broadening is observed with increased $RhCl_3$ content in the precursor solutions. From the peak width in PXRD patterns of Rh-6.4/SBA-15 and Rh-3.2/SBA-15, we calculated their respective average particle sizes of 6.1 and 3.0 nm using the Debye-Scherrer equation. The PXRD peak broadening of Rh-1.6/SBA-15 is too great for Rh peaks to be clearly observed, as is expected for NPs smaller than 2 nm at this metal loading. The amount of surface-exposed Rh was determined as 18% for Rh-6.4/SBA-15, 30% for Rh-3.2/SBA-15, and 70% for Rh-1.6/SBA-15 according to CO chemisorption. The measured dispersions match well with the predicted values based on average particle sizes for each catalyst.

Table 1. Loading of Rh-X/SBA-15 catalysts as measured by ICP-MS.

Catalyst	Actual Loading (Rh wt.%)	Loading after Catalysis (Rh wt.%)
Rh-1.6/SBA-15	3.0 ± 0.1	3.0 ± 0.1
Rh-3.2/SBA-15	3.1 ± 0.1	3.1 ± 0.1
Rh-6.4/SBA-15	3.1 ± 0.2	3.0 ± 0.2

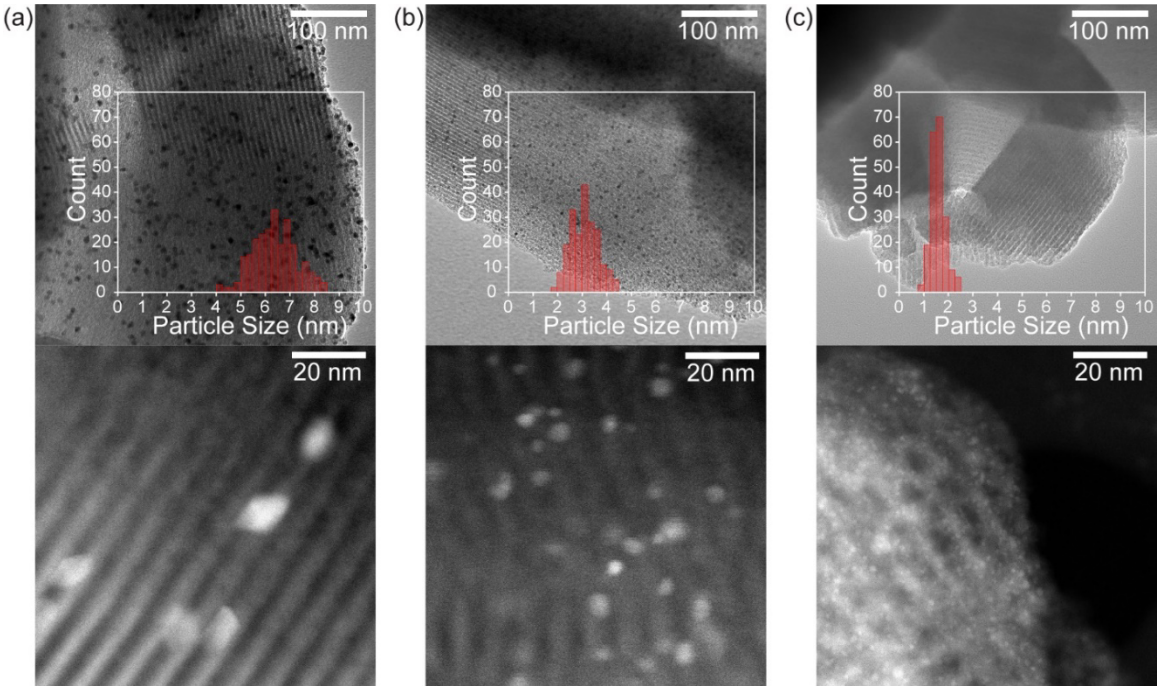

Figure 1. TEM (**top row**) and STEM (**bottom row**) images of SBA-15-supported Rh nanoparticles of different sizes, Rh-X/SBA-15, where X is the averaged Rh particle size: (**a**) X = 6.4 ± 0.9 nm, (**b**) X = 3.2 ± 0.6 nm, and (**c**) X = 1.6 ± 0.3 nm. Insets are histograms of measured particle sizes.

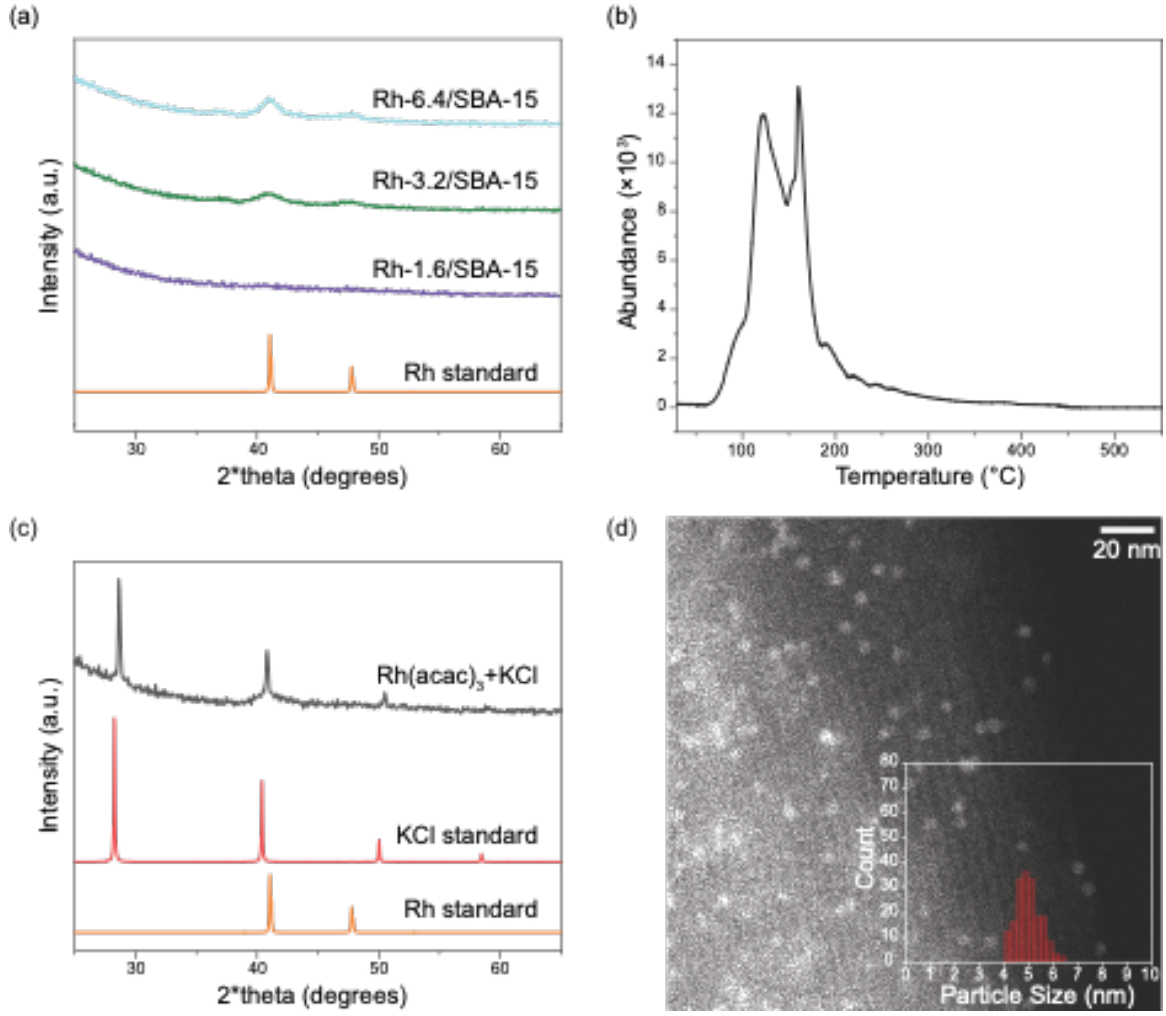

Figure 2. Characterization of the Rh-X/SBA-15 catalysts and the effect of Cl^- from KCl on the size of Rh NPs. (**a**) PXRD patterns for each NP size. (**b**) H_2-TPR of unreduced $RhCl_3$/SBA-15. (**c**) PXRD and (**d**) STEM of $Rh(acac)_3$/SBA-15 reduced in the presence of KCl with a ratio of Rh:Cl = 1:3. Inset in (**d**) is the size histogram of Rh NPs. Reduction condition: 10% H_2 in He was flowed at 50 mL/min, starting at 30 °C and ramping at 5 °C/min.

We propose two potential explanations for the disparity in NP size between the two Rh precursor salts. First, the physical differences between the precursor salts could lead to different interactions with the support. In $Rh(acac)_3$, the rhodium atom is capped inside a relatively large organic ligand, which would interact weakly with surface hydroxyls on SBA-15. Weaker interactions of $Rh(acac)_3$ molecules with the support would lead to their higher mobility on the support, enabling faster aggregation. Conversely, $RhCl_3$ can dissociate in an aqueous solution, and interactions between rhodium ions and support hydroxyls could be much stronger, leading to more nucleation centers and smaller particles rather than aggregation during the reduction. The second possibility for the size discrepancy is a change in the mechanism of NP formation induced by Cl^- or HCl formed during the reduction step when $RhCl_3$ is loaded into the support. It was previously reported that HCl could redisperse metal atoms in a supported catalyst [31]. A higher ratio of Cl/Pt present during reduction led to higher metal dispersion. However, no mechanistic insights were provided in that report.

If HCl does play a role in forming the smaller particle size, the first possibility would be the prevention of NP nucleation. Another step in NP growth potentially hindered by HCl could be aggregation. Inhibiting diffusion and aggregation or inducing redispersion of aggregated atoms would slow the growth process and result in smaller NPs. To probe the role of HCl in Rh-1.6/SBA-15, we performed H_2-TPR experiments (Figure 2b) measuring the release of m/z = 36.5 (HCl). The first detection of HCl peaks at 130 °C, likely the release of HCl as reduction of Rh begins. There is a second peak at 170 °C, which we believe could be the desorption of HCl from Rh atoms or NPs. The elution of HCl lasts until 300 °C, which suggests that HCl could facilitate the dispersion of Rh during the reduction at 200 °C. Further work is still needed to identify the exact mechanism, nucleation or redispersion, by which particle size is affected between the chloride and acetylacetonate salts. Still, the identification of HCl desorption indicates that it could play a role in limiting particle growth during reduction. The ability of chloride to

promote NP dispersion was also investigated by adding another Cl^- source, KCl, to $Rh(acac)_3$/SBA-15 before the reduction step. PXRD of the reduced sample shows strong diffraction peaks from undecomposed KCl (Figure 2c). Without Cl^-, the reduction of this sample leads to 6.4 ± 0.9 nm Rh NPs. With the inclusion of KCl, we observed a decrease in the average particle size to 4.9 ± 0.6 nm (Figure 2d). This result indicates that KCl is less effective than the Cl^- in $RhCl_3$ in reducing Rh NPs size, possibly due to the physical separation of the Rh^{3+} and Cl^- salts.

The Rh K-edge X-ray absorption near-edge spectrum (XANES) is shown in Figure 3a. The XANES energy is the inflection point of the leading edge; the energy of Rh-6.4/SBA-15 and Rh-3.2/SBA-15 is 23.2200 keV, very close to the foil at 23.2208 keV (Table 2), indicating a high fraction of metallic Rh. For Rh-6.4/SBA-15, the shape of the XANES is also nearly identical to the foil, while in Rh-3.2/SBA-15, there is a slight increase in the white line intensity, the first peak in the XANES spectrum, which indicates partially oxidized Rh NPs. The XANES energy of Rh-1.6/SBA-15 is at 23.2286 keV, indicating these NPs are more highly oxidized. The fraction of metallic and oxidized Rh was determined by fitting the sample XANES with Rh foil and Rh_2O_3, and the fits are given in Table 2. The fraction of Rh^{3+} in Rh-1.6/SBA-15 and Rh-3.2/SBA-15 was 69% and 37%, respectively, while the fraction of oxidized Rh in Rh-6.4/SBA-15 was too small to detect in these larger particles. The amount of oxidized Rh in Rh-1.6/SBA-15 and Rh-3.2/SBA-15 is close to the dispersion for each catalyst.

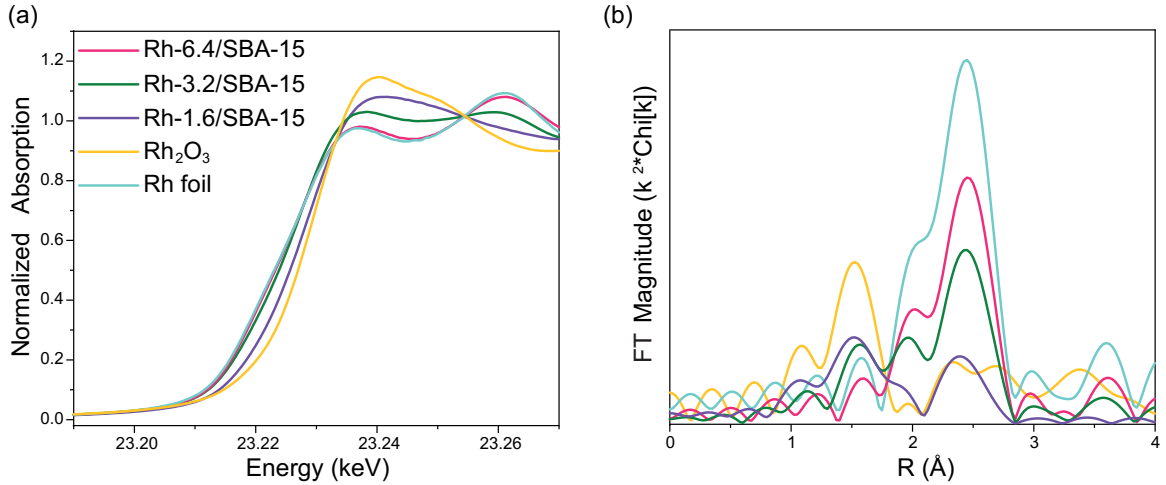

Figure 3. X-ray absorption spectroscopy results for (**a**) X-ray absorption near edge region, and (**b**) Fourier transformation of extended fine structure region.

Table 2. XAS fitting parameters.

Sample	k-Edge Energy (keV)	Rh^{3+} (%)	Rh^0 (%)	Scatter Path	CN	R (Å)	σ^2	E_0 (eV)
Rh Foil	23.2208	-	100	Rh-Rh	12	2.69	0.004	0.8
Rh_2O_3 Standard	23.2305	100	-	Rh-O	6	2.05	0.005	−4.4
Rh-1.6/SBA-15	23.2286	69	31	Rh-O	3.3	2.05	0.005	−1.3
				Rh-Rh	2.0	2.68	0.004	−1.5
Rh-3.2/SBA-15	23.2200	37	63	Rh-O	2.0	2.05	0.005	7.0
				Rh-Rh	5.4	2.69	0.004	2.7
Rh-6.4/SBA-15	23.2200	-	-	Rh-O	-	-	-	-
				Rh-Rh	7.5	2.69	0.004	2.1

The k^2-weighted magnitude of the Fourier transforms of the extended x-ray absorption fine structure (EXAFS) data are shown in Figure 3b. The peaks (phase uncorrected distances) at about 1.0 to 1.9 Å are due to Rh-O scattering, while the multiple peaks from about 1.5 to 3.0 Å are due to Rh-Rh scattering. As the Rh NP size decreases, there is a decrease in the size of the Rh-Rh peak and an increase in the size of the Rh-O peak. The EXAFS fits are given in Table 2. For Rh-6.4/SBA-15, the Rh-Rh coordination number (CN) was 7.5 at a bond distance of 2.69 Å, consistent with metallic Rh NPs. No Rh-O scattering peak is observed in this sample. For Rh-3.2/SBA-15, there are both Rh-O, CN = 2.0 at 2.05 Å, and Rh-Rh, CN = 5.4 at 2.69 Å, peaks indicating partially oxidized Rh NPs. For Rh-1.6/SBA-15, the Rh-O CN increases to 3.3 at 2.05 Å, and the Rh-Rh CN decreases to 2.0 at 2.68 Å. Two factors contribute to the decrease in Rh-Rh scattering as particle size decreases. First, the Rh coordination number decreases with particle size [34], leading to lower scattering intensity. Second, there is a higher proportion of surface atoms in smaller NPs; thus, a larger fraction of metallic Rh is oxidized as the size decreases.

After the observations of the potential surface oxidation of the catalysts, fresh catalysts were prepared and kept in a strictly oxygen-free environment until they were unsealed for immediate XPS analysis (Figure 4). The deconvoluted Rh 3d XPS spectra of three catalysts revealed the presence of both metallic Rh and Rh oxide species. By quantifying the peak areas, the relative proportions of surface oxide were determined to be 18%, 30%, and 42% for Rh-6.4/SBA-15, Rh-3.2/SBA-15, and Rh-1.6/SBA-15, respectively (Table 3). These findings suggest that the oxidation of Rh occurs rapidly upon exposure to air, agreeing with XAS analyses.

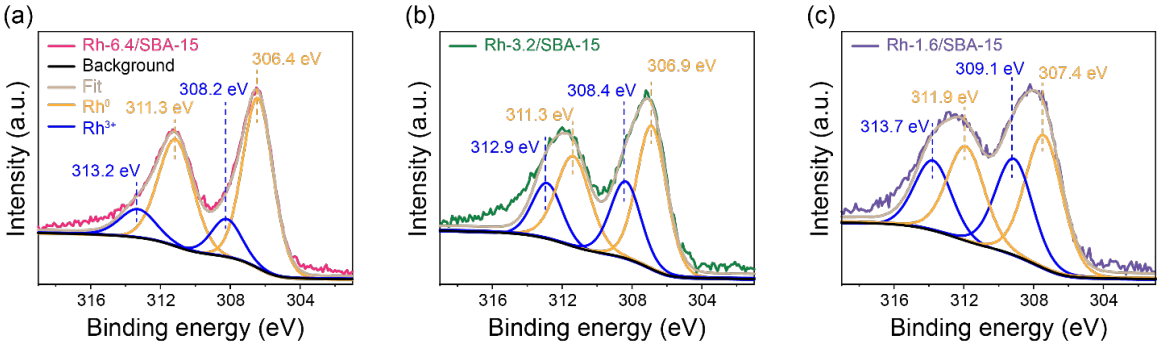

Figure 4. Rh 3d XPS spectra of (**a**) Rh-6.4/SBA-15, (**b**) Rh-3.2/SBA-15, (**c**) Rh-1.6/SBA-15.

Table 3. XPS fitting information.

Catalyst	Rh^{3+} $3d_{5/2}$ Binding Energy (eV)	Rh^{0} $3d_{5/2}$ Binding Energy (eV)	Rh^{3+} $3d_{5/2}$ Peak Area	Rh^{0} $3d_{5/2}$ Peak Area
Rh-1.6/SBA-15	309.1	307.4	0.72	1.00
Rh-3.2/SBA-15	308.4	306.9	0.54	1.00
Rh-6.4/SBA-15	308.2	306.4	0.22	1.00

DRIFTS of adsorbed CO was used to investigate the catalysts' surfaces [35–37]. Since the XAS and XPS showed that these NPs are easily oxidized in air, samples were pretreated with 10% H_2 at 200 °C before performing DRIFTS measurements shown in Figure 5. Rh-1.6/SBA-15 and Rh-3.2/SBA-15 have similar intensities for bridged-bonded CO peaks at ~1900 cm^{-1}, while the linear peak at 2063 cm^{-1} of Rh-3.2/SBA-15 is much smaller. Only linearly adsorbed CO is observed on Rh-6.4/SBA-15 after 10 min of flushing out CO. Once the 20 min were completed, no gaseous CO can be observed, while the amount of adsorbed CO remains the same. CO adsorbed on Rh-6.4/SBA-15 during the experiment was likely much lower than in the other catalysts, leading the bridged and most linear bonded CO to desorb quickly when CO was shut off.

Bridged CO adsorption peaks have previously been attributed to terrace atoms on NP surfaces [38]. The similar peak areas of bridged CO adsorption in Rh-1.6/SBA-15 and Rh-3.2/SBA-15 suggest that these catalysts have only a small difference in the number of terrace atoms on their surfaces. Conversely, the linear adsorption peak has been assigned to adsorption onto corner and edge atoms. The large difference in linearly adsorbed CO corresponds to a much greater number of corners and edges on Rh-1.6/SBA-15 than on Rh-3.2/SBA-15, consistent with smaller NPs. In Rh-1.6/SBA-15 and Rh-3.2/SBA-15, there is a CO vibration peak at 2090 cm^{-1} and a shoulder at 2024 cm^{-1} due to the symmetric and asymmetric stretching of gem-dicarbonyl (geminal) $Rh(CO)_2$. Geminal peaks are characteristic of positive or partially positive Rh atoms, including atomically isolated Rh. These peaks are likely caused by interactions of CO with the edges and corners, causing the particles to redisperse [39]. This does not interfere with hydroformylation reactions, as the syngas is overall reducing for the NPs; also, as demonstrated in Table 1, the catalysts do not leach Rh under the hydroformylation conditions.

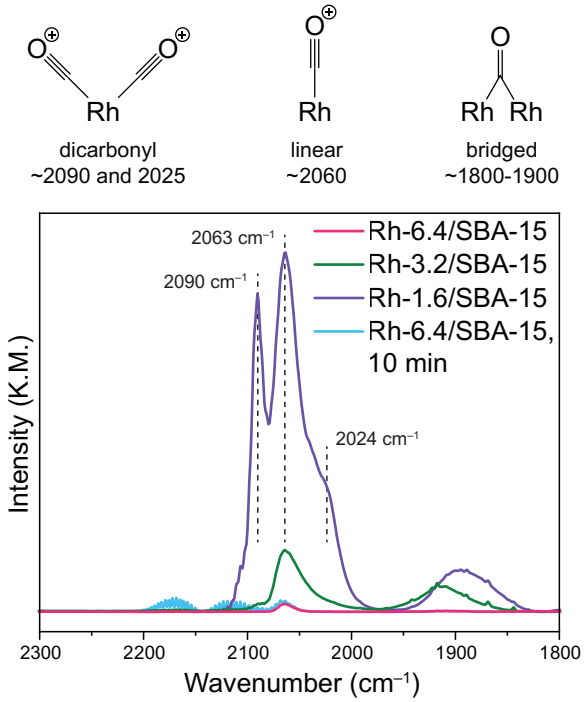

Figure 5. CO-DRIFTS spectra from each of the three materials. 5 mL/min CO diluted with 20 mL/min He was flowed for 20 min, after which time CO was turned off, and the sample was flushed for another 20 min before collecting reported spectra. The additional spectrum of Rh-6.4/SBA-15 is after only 10 min of flushing as indicated, which shows clear gas phase CO.

After characterizing the size-controlled Rh catalysts, the catalytic performance for the hydroformylation of styrene at low temperatures was determined. Hydroformylation is typically performed at 90–110 °C. Because of the high activity of Rh-1.6/SBA-15 with our previously reported conditions [13], we studied low-temperature hydroformylation. To compare the difference in activity, total styrene conversion was kept at ~10% for each catalytic reaction. At 50 °C, Rh-1.6/SBA-15 is approximately 2.5 times more active than Rh-3.2/SBA-15 and five times more active than Rh-6.4/SBA-15 by comparing TOFs (Figure 6a, Table 4), consistent with previous studies of Rh NP size [30]. All three catalysts surpass the performance of the benchmark Wilkinson catalyst. The activation energies were determined using Arrhenius plots within a temperature window of 50–80 °C (Figure 6b). The energy barrier for Rh-1.6/SBA-15 is lower than that of the other catalysts. We attribute the high activity of Rh-1.6/SBA-15 to the increased fraction of lower coordinated edge and corner sites, which turn over more quickly than the terraces on the NPs, matching previously reported trends.

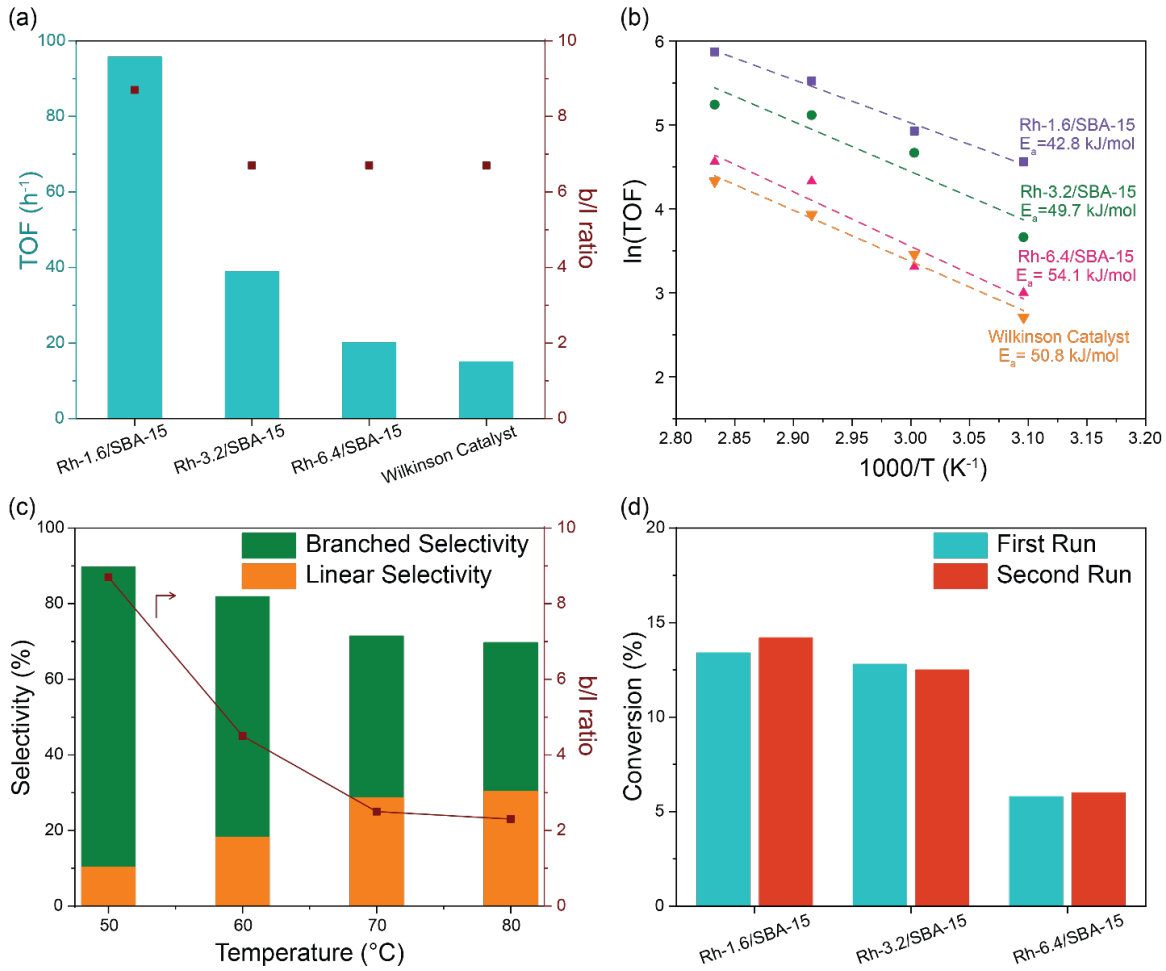

Figure 6. (**a**) Synthesized and Wilkinson catalysts compared by TOF and branched to linear ratio (b/l) at 50 °C; Rh-1.6/SBA-15, Rh-3.2/SBA-15, and Wilkinson catalyst ran for 2 h, Rh-6.4/SBA-15 ran for 16 h. (**b**) Arrhenius plot calculating activation energy. (**c**) Trend of b/l over Rh-1.6/SBA-15 at ~10% conversion at different temperatures, 60 °C for 1.5 h, 70 °C for 1 h, 80 °C for 0.5 h. (**d**) Recycle tests for all the heterogeneous catalysts. Rh-1.6/SBA-15 ran for 2 h, all others for 16 h. Reaction conditions: 0.5 mmol styrene, 0.5 µmol total Rh, 30 bar syngas, 2 mL toluene.

Table 4. Hydroformylation of styrene over rhodium catalysts.

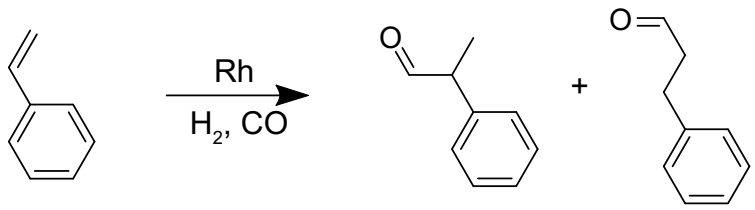

Entry	Catalyst	Time (h)	Conversion (%)	TOF (h^{-1})	b/l
1	Rh-1.6/SBA-15	2	13.4	95.7	8.7
2	Rh-3.2/SBA-15	2	2.8	38.9	6.8
3	Rh-6.4/SBA-15	16	5.6	20.1	6.8
4	Wilkinson Catalyst	2	3.0	15.0	6.8

Reaction conditions: 0.5 mmol styrene, 0.5 µmol Rh, 2 mL toluene, 30 bar syngas, 50 °C.

We also studied the impact of the reaction temperature on regioselectivity over Rh-1.6/SBA-15 (Figure 6c). We found that as reaction temperature decreased, the preference toward the production of the branched product increased, agreeing with previous studies on the hydroformylation of various olefins [40]. Additionally, the Wilkinson catalyst gave a similar branched to linear (b/l) ratio as the supported NPs, further confirming the observed regioselectivity is due to reaction conditions and not catalyst structure, as observed previously [18]. We conducted recycle tests of each catalyst by washing it with ethanol post-reaction and then collecting the solid

catalyst by centrifugation. The recycle tests show no activity loss upon reusing each catalyst (Figure 6d), agreeing with the ICP-MS results that show no Rh leaching (Table 1).

After catalysis, we performed CO-DRIFTS on used catalysts to investigate potential changes in the NP structures during catalytic reactions (Figure 7). Previous reports have demonstrated dispersion of rhodium NPs upon exposure to CO [35,41]. The spectra of Rh-3.2/SBA-15 and Rh-6.4/SBA-15 are entirely unchanged, indicating no structural changes in Rh NPs of used catalysts. We again included an earlier spectrum of Rh-6.4/SBA-15 (10 min He purge) as the baseline changes in the latter 10 min of the typical scan. Rh-1.6/SBA-15 no longer has a clearly visible bridged CO peak, indicating a slight decrease in the particle size during the reaction. Rh NPs of 1 nm and smaller have been reported to lack the bridged CO peak [41]. The symmetric and asymmetric stretching peaks of gem-dicarbonyl (geminal) $Rh(CO)_2$ on Rh-1.6/SBA-15 are also weakened, indicating the number of single atom Rh is also reduced during catalysis.

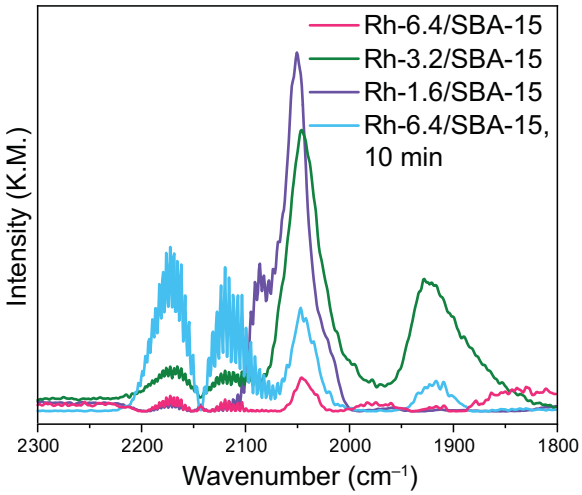

Figure 7. CO-DRIFTS spectra of used catalysts. Reaction conditions: 2.0 mmol styrene, 2.0 µmol total Rh, 30 bar syngas, 8 mL toluene, 2 h, 50 °C. CO-DRIFTS experiments were performed following the same procedures used to obtain spectra in Figure 5.

We evaluated Rh-1.5/SBA-15 for the hydroformylation of 1-isobutyl-4-vinylbenzene, following a previous method by Gao et al. [18] (Scheme 2). After hydroformylation, the resulting branched aldehyde can be further oxidized to make the active ingredient of ibuprofen, which is sold as a racemic mixture. Following the previously reported conditions, we could not match their 92% yield to the branched product in a toluene-water (50:50) mixed solvent. By switching the solvent mixture to pure toluene rather than a 50% mixture with water, we achieved a yield of 92%, with a b/l = 12/1. A possible reason is that the substrate is insoluble in water, and the SBA-15 support likely stays in the aqueous phase due to surface hydroxyls.

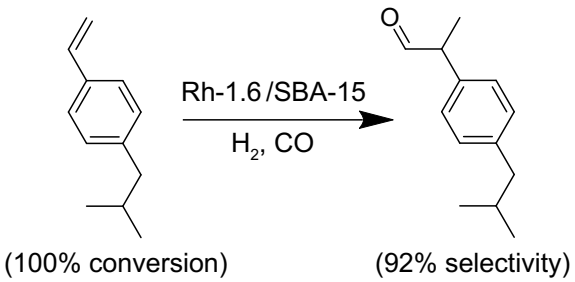

Scheme 2. Reaction scheme for the hydroformylation of 1-isobutyl-4-vinylbenzne. Reaction conditions: 0.4 mmol 1-isobutyl-4-vinylbenzene, 0.5 µmol total Rh, 30 bar syngas, 3 mL toluene, 40 °C, 24 h.

In addition to the control of Rh NP size, the applicability of our synthesis method was demonstrated for other noble metals, e.g., Pt and Pd. Using K_2MCl_4 salts where M = Pt or Pd, we could again achieve high dispersion, with particle sizes <2 nm from PXRD measurements (Figure 8). For the preparation with a mixture of Cl^- and acetylacetonate salts, the peaks were more prominent, though still small, and synthesis with only acetylacetonate salts formed much larger NPs. The NPs formed from platinum (II) acetylacetonate had a Debye-Scherrer particle size of 11 nm, while the $Pd(acac)_2$ salt yielded 8 nm particles. The larger particles from acetylacetonate salts allow

for the possibility of controlling the NP size over an increased range depending on the ratio of chloride to acetylacetonate salt.

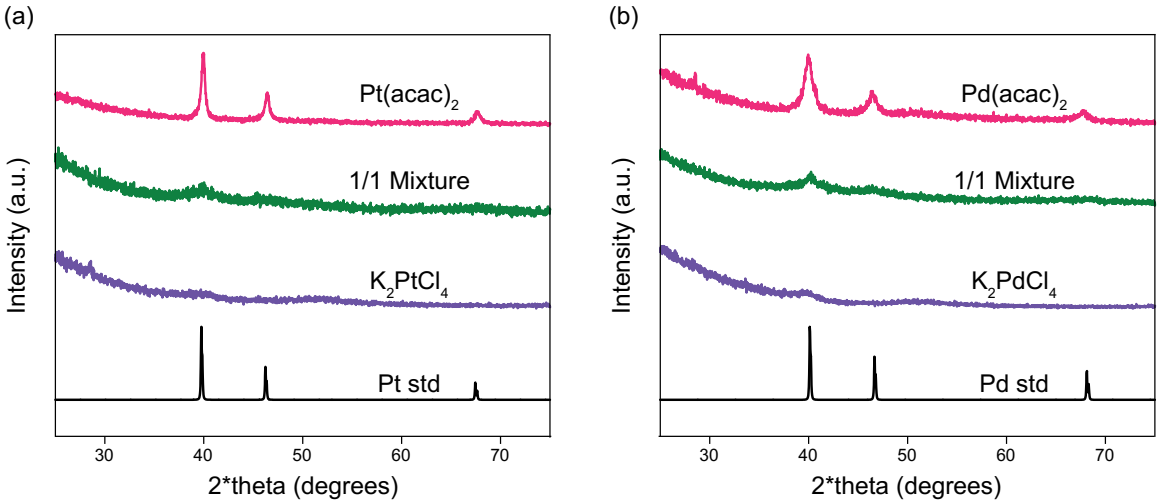

Figure 8. PXRD patterns of (**a**) Pt and (**b**) Pd NPs synthesized according to the method developed for rhodium display a similar trend.

4. Conclusion

Controlling NP sizes while accounting for metal loading and dispersion measurements and keeping the catalysts clean of bulky ligands is a valuable way to study the effect of particle size on reaction systems. We have applied a method of tuning the chloride content by adjusting the ratio of two precursors to affect the particle size of Rh NPs. The size-controlled Rh/SBA-15 catalysts were used to study the size-dependent nature of styrene hydroformylation. Using STEM, we identified a clear trend of NP size increase with decreasing chloride salt content used during the impregnation. PXRD and XAS studies confirmed that the bulk of our material follows that trend. Surface structures of these particles are also characterized by XPS and CO-DRIFTS. When applying these catalysts to hydroformylation, there is a clear activity increase with the decrease of Rh NP size. This reinforces the hypothesis based on small molecule hydroformylation that styrene hydroformylation would depend on particle size. Unlike the hydroformylation of small molecules, where <2 nm NPs tend to hydrogenate olefins, Rh-1.6/SBA-15 was 100% chemoselective to aldehyde products in styrene hydroformylation. This high selectivity and temperature-dependent regioselectivity to the branched aldehyde allowed us to synthesize the branched aldehyde precursor of ibuprofen efficiently. Finally, we demonstrated the applicability of this simple size control method to Pt and Pd, two other essential metals heavily used in catalysis.

Author Contributions

A.L.: conceptualization, methodology, writing—original draft preparation, reviewing and editing, TEM imaging, visualization, investigation; C.J.W.: XAS data collection, writing—reviewing and editing, visualization, software; J.T.M.: XAS data fitting; Z.A.: XPS data collection; X.L.: XPS data fitting; J.T.: organic synthesis; R.C.: STEM imaging; X.W.: STEM imaging; L.M.S.: guiding the organic synthesis; W.H.: conceptualization, guiding the research, writing—reviewing and editing. All authors have read and agreed to the published version of the manuscript.

Data Availability Statement

Raw data will be made available upon reasonable request.

Acknowledgments

This work is supported by National Science Foundation grant CHE-2108307 and Iowa State University Trapp Award. This research used beamline 8-ID ISS of the National Synchrotron Light Source II, a U.S. Department of Energy (DOE) Office of Science User Facility operated for the DOE Office of Science by Brookhaven National Laboratory under Contract No. DE-SC0012704. Z.A. acknowledges the support from Qassim University. X.L. is grateful for the support from DOE Early Career Research Program (DE-SC0022000).

Conflicts of Interest

The authors declare no conflict of interest.

References

1. Xu, L.; Liu, D.; Chen, D.; et al. Size and Shape Controlled Synthesis of Rhodium Nanoparticles. *Heliyon* **2019**, *5*, e01165. https://doi.org/10.1016/j.heliyon.2019.e01165.
2. Yang, F.; Deng, D.; Pan, X.; et al. Understanding Nano Effects in Catalysis. *Natl. Sci. Rev.* **2015**, *2*, 183–201. https://doi.org/10.1093/nsr/nwv024.
3. Cuenya, B.R. Synthesis and Catalytic Properties of Metal Nanoparticles: Size, Shape, Support, Composition, and Oxidation State Effects. *Thin Solid. Films* **2010**, *518*, 3127–3150. https://doi.org/10.1016/j.tsf.2010.01.018.
4. Suchomel, P.; Kvitek, L.; Prucek, R.; et al. Simple Size-Controlled Synthesis of Au Nanoparticles and Their Size-Dependent Catalytic Activity. *Sci. Rep.* **2018**, *8*, 4589. https://doi.org/10.1038/s41598-018-22976-5.
5. Alabdullah, M.; Ibrahim, M.; Dhawale, D.; et al. Rhodium Nanoparticle Size Effects on the CO_2 Reforming of Methane and Propane. *ChemCatChem* **2021**, *13*, 2879–2886. https://doi.org/10.1002/cctc.202100063.
6. Chen, M.; Han, Y.; Wei Goh, T.; et al. Kinetics, Energetics, and Size Dependence of the Transformation from Pt to Ordered PtSn Intermetallic Nanoparticles. *Nanoscale* **2019**, *11*, 5336–5345. https://doi.org/10.1039/C8NR10067E.
7. Humphrey, S.M.; Grass, M.E.; Habas, S.E.; et al. Rhodium Nanoparticles from Cluster Seeds: Control of Size and Shape by Precursor Addition Rate. *Nano Lett.* **2007**, *7*, 785–790. https://doi.org/10.1021/nl070035y.
8. Wang, C.; Li, Y.; Zhang, C.; et al. A Simple Strategy to Improve Pd Dispersion and Enhance Pd/TiO_2 Catalytic Activity for Formaldehyde Oxidation: The Roles of Surface Defects. *Appl. Catal. B Environ.* **2021**, *282*, 119540. https://doi.org/10.1016/j.apcatb.2020.119540.
9. Wu, X.; Tennakoon, A.; Yappert, R.; et al. Size-Controlled Nanoparticles Embedded in a Mesoporous Architecture Leading to Efficient and Selective Hydrogenolysis of Polyolefins. *J. Am. Chem. Soc.* **2022**, *144*, 5323–5334. https://doi.org/10.1021/jacs.1c11694.
10. Luo, L.; Li, H.; Peng, Y.; et al. Rh-Based Nanocatalysts for Heterogeneous Reactions. *ChemNanoMat* **2018**, *4*, 451–466. https://doi.org/10.1002/cnma.201800033.
11. Zhang, Y.; Grass, M.E.; Kuhn, J.N.; et al. Highly Selective Synthesis of Catalytically Active Monodisperse Rhodium Nanocubes. *J. Am. Chem. Soc.* **2008**, *130*, 5868–5869. https://doi.org/10.1021/ja801210s.
12. Han, D.; Li, X.; Zhang, H.; et al. Heterogeneous Asymmetric Hydroformylation of Olefins on Chirally Modified Rh/SiO_2 Catalysts. *J. Catal.* **2006**, *243*, 318–328. https://doi.org/10.1016/j.jcat.2006.08.003.
13. Chen, M.; Gupta, G.; Ordonez, C.W.; et al. Intermetallic Nanocatalyst for Highly Active Heterogeneous Hydroformylation. *J. Am. Chem. Soc.* **2021**, *143*, 20907–20915. https://doi.org/10.1021/jacs.1c09665.
14. Munnik, P.; de Jongh, P.E.; de Jong, K.P. Recent Developments in the Synthesis of Supported Catalysts. *Chem. Rev.* **2015**, *115*, 6687–6718. https://doi.org/10.1021/cr500486u.
15. García-Sánchez, J.T.; Valderrama-Zapata, R.; Acevedo-Córdoba, L.F.; et al. Calculation of Mass Transfer Limitations for a Gas-Phase Reaction in an Isothermal Fixed Bed Reactor: Tutorial and Sensitivity Analysis. *ACS Catal.* **2023**, *13*, 6905–6918. https://doi.org/10.1021/acscatal.3c01282.
16. Franke, R.; Selent, D.; Börner, A. Applied Hydroformylation. *Chem. Rev.* **2012**, *112*, 5675–5732. https://doi.org/10.1021/cr3001803.
17. Lang, R.; Li, T.; Matsumura, D.; et al. Hydroformylation of Olefins by a Rhodium Single-Atom Catalyst with Activity Comparable to $RhCl(PPh_3)_3$. *Angew. Chem. Int. Ed.* **2016**, *55*, 16054–16058. https://doi.org/10.1002/anie.201607885.
18. Gao, P.; Liang, G.; Ru, T.; et al. Phosphorus Coordinated Rh Single-Atom Sites on Nanodiamond as Highly Regioselective Catalyst for Hydroformylation of Olefins. *Nat. Commun.* **2021**, *12*, 4698. https://doi.org/10.1038/s41467-021-25061-0.
19. Tudor, R.; Shah, A. Industrial Low Pressure Hydroformylation: Forty-Five Years of Progress for the LP OxoSM Process. *Johns. Matthey Technol. Rev.* **2017**, *61*, 246–256. https://doi.org/10.1595/205651317X695875.
20. Hanf, S.; Alvarado Rupflin, L.; Gläser, R.; et al. Current State of the Art of the Solid Rh-Based Catalyzed Hydroformylation of Short-Chain Olefins. *Catalysts* **2020**, *10*, 510. https://doi.org/10.3390/catal10050510.
21. Liu, Y.; Zhao, J.; Zhao, Y.; et al. Homogeneous Hydroformylation of Long Chain Alkenes Catalyzed by Water Soluble Phosphine Rhodium Complex in CH_3OH and Efficient Catalyst Cycling. *RSC Adv.* **2019**, *9*, 7382–7387. https://doi.org/10.1039/C8RA08787C.
22. Wang, P.; Shi, H.; Feng, B.; et al. Highly Selective and Recyclable Homogeneous Hydroformylation of Olefins with $[Rh(Cod)Cl]_2/PPh_3$ Regulated by Et3N as Additive. *Mol. Catal.* **2023**, *548*, 113459. https://doi.org/10.1016/j.mcat.2023.113459.

23. Evans, D.; Osborn, J.A.; Wilkinson, G. Hydroformylation of Alkenes by Use of Rhodium Complex Catalysts. *J. Chem. Soc. Inorg. Phys. Theor.* **1968**, 3133–3142. https://doi.org/10.1039/J19680003133.
24. Brown, C.K.; Wilkinson, G. Homogeneous Hydroformylation of Alkenes with Hydridocarbonyltris-(Triphenylphosphine)Rhodium(I) as Catalyst. *J. Chem. Soc. Inorg. Phys. Theor.* **1970**, 2753–2764. https://doi.org/10.1039/J19700002753.
25. Bohnen, H.-W.; Cornils, B. Hydroformylation of Alkenes: An Industrial View of the Status and Importance. In *Advances in Catalysis*; Academic Press: Cambridge, MA, USA, 2002; Volume 47, pp. 1–64.
26. Han, D.; Li, X.; Zhang, H.; et al. Asymmetric Hydroformylation of Olefins Catalyzed by Rhodium Nanoparticles Chirally Stabilized with (R)-BINAP Ligand. *J. Mol. Catal. Chem.* **2008**, *283*, 15–22. https://doi.org/10.1016/j.molcata.2007.12.008.
27. Bruss, A.J.; Gelesky, M.A.; Machado, G.; et al. Rh(0) Nanoparticles as Catalyst Precursors for the Solventless Hydroformylation of Olefins. *J. Mol. Catal. Chem.* **2006**, *252*, 212–218. https://doi.org/10.1016/j.molcata.2006.02.063.
28. McClure, S.M.; Lundwall, M.J.; Goodman, D.W. Planar Oxide Supported Rhodium Nanoparticles as Model Catalysts. *Proc. Natl. Acad. Sci. USA* **2011**, *108*, 931–936. https://doi.org/10.1073/pnas.1006635107.
29. Yang, Q.; Wang, P.; Li, C.; et al. Unravelling Structure Sensitivity in Heterogeneous Hydroformylation of Aldehyde over Rh. *Chem. Eng. J.* **2024**, *481*, 148529. https://doi.org/10.1016/j.cej.2024.148529.
30. Hanaoka, T.; Arakawa, H.; Matsuzaki, T.; et al. Ethylene Hydroformylation and Carbon Monoxide Hydrogenation over Modified and Unmodified Silica Supported Rhodium Catalysts. *Catal. Today* **2000**, *58*, 271–280. https://doi.org/10.1016/S0920-5861(00)00261-3.
31. Barbier, J.; Bahloul, D.; Marecot, P. Reduction of Pt/Al_2O_3 Catalysts: Effect of Hydrogen and of Water and Hydrochloric Acid Vapor on the Accessibility of Platinum. *J. Catal.* **1992**, *137*, 377–384. https://doi.org/10.1016/0021-9517(92)90165-E.
32. Zhao, D.; Feng, J.; Huo, Q.; et al. Triblock Copolymer Syntheses of Mesoporous Silica with Periodic 50 to 300 Angstrom Pores. *Science* **1998**, *279*, 548–552. https://doi.org/10.1126/science.279.5350.548.
33. Greenhalgh, M.D.; Thomas, S.P. Iron-Catalyzed, Highly Regioselective Synthesis of α-Aryl Carboxylic Acids from Styrene Derivatives and CO2. *J. Am. Chem. Soc.* **2012**, *134*, 11900–11903. https://doi.org/10.1021/ja3045053.
34. Marinkovic, N.S.; Sasaki, K.; Adzic, R.R. Determination of Single- and Multi-Component Nanoparticle Sizes by X-ray Absorption Spectroscopy. *J. Electrochem. Soc.* **2018**, *165*, J3222. https://doi.org/10.1149/2.0281815jes.
35. Asokan, C.; Xu, M.; Dai, S.; et al. Synthesis of Atomically Dispersed Rh Catalysts on Oxide Supports via Strong Electrostatic Adsorption and Characterization by Cryogenic Infrared Spectroscopy. *J. Phys. Chem. C* **2022**, *126*, 18704–18715. https://doi.org/10.1021/acs.jpcc.2c05426.
36. Yang, C.; Garl, C.W. Infrared Studies of Carbon Monoxide Chemisorbed on Rhodium. *J. Phys. Chem.* **1957**, *61*, 1504–1512. https://doi.org/10.1021/j150557a013.
37. Chen, M.; Yan, Y.; Gebre, M.; et al. Thermal Unequilibrium of PdSn Intermetallic Nanocatalysts: From In Situ Tailored Synthesis to Unexpected Hydrogenation Selectivity. *Angew. Chem. Int. Ed.* **2021**, *60*, 18309–18317. https://doi.org/10.1002/anie.202106515.
38. Meng, X.; Yang, Y.; Chen, L.; et al. A Control over Hydrogenation Selectivity of Furfural via Tuning Exposed Facet of Ni Catalysts. *ACS Catal.* **2019**, *9*, 4226–4235. https://doi.org/10.1021/acscatal.9b00238.
39. Marino, S.; Wei, L.; Cortes-Reyes, M.; et al. Rhodium Catalyst Structural Changes during, and Their Impacts on the Kinetics of, CO Oxidation. *JACS Au* **2023**, *3*, 459–467. https://doi.org/10.1021/jacsau.2c00595.
40. Caiazzo, A.; Settambolo, R.; Uccello-Barretta, G.; et al. Influence of the Reaction Temperature on the Regioselectivity in the Rhodium-Catalyzed Hydroformylation of Vinylpyrroles. *J. Organomet. Chem.* **1997**, *548*, 279–284. https://doi.org/10.1016/S0022-328X(97)00479-8.
41. Yan, G.; Tang, Y.; Li, Y.; et al. Reaction Product-Driven Restructuring and Assisted Stabilization of a Highly Dispersed Rh-on-Ceria Catalyst. *Nat. Catal.* **2022**, *5*, 119–127. https://doi.org/10.1038/s41929-022-00741-2.